

Growth Mechanism and Electronic Structure of Zn₃P₂ on the Ga-Rich GaAs(001) Surface

Seokmin Jeon,[†] Jeffrey P. Bosco,[†] Samantha S. Wilson,[†] Steve J. Rozeveld,[‡] Hyungjun Kim,[§] and Harry A. Atwater^{*,†}

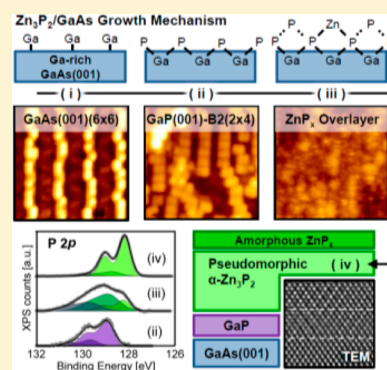
[†]Thomas J. Watson Laboratories of Applied Physics, California Institute of Technology, MC 128-95, Pasadena, California 91125, United States

[‡]Analytical Sciences Laboratory, Dow Chemical Company, Midland, Michigan 48674, United States

[§]Graduate School of EEWS, Korea Advanced Institute of Science and Technology (KAIST), Daejeon 305-701, Republic of Korea

S Supporting Information

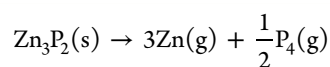
ABSTRACT: The growth of epitaxial Zn₃P₂ films on III–V substrates unlocks a promising pathway toward high-efficiency, earth-abundant photovoltaic devices fabricated on reusable, single-crystal templates. The detailed chemical, structural, and electronic properties of the surface and interface of pseudomorphic Zn₃P₂ epilayers grown on GaAs(001) were investigated using scanning tunneling microscopy/spectroscopy and high-resolution X-ray photoelectron spectroscopy. Two interesting features of the growth process were observed: (1) vapor-phase P₄ first reacts with the Ga-rich GaAs surface to form an interfacial GaP layer with a thickness of several monolayers, and (2) a P-rich amorphous overlayer is present during the entire film growth process, beneath which a highly ordered Zn₃P₂ crystalline phase is precipitated. These features were corroborated by transmission electron micrographs of the Zn₃P₂/GaAs interface as well as density functional theory calculations of P reactions with the GaAs surface. Finally, the valence-band offset between the crystalline Zn₃P₂ epilayer and the GaAs substrate was determined to be $\Delta E_V = 1.0 \pm 0.1$ eV, indicating the formation of a hole-depletion layer at the substrate surface which may inhibit formation of an ohmic contact.



1.0. INTRODUCTION

Zinc phosphide (Zn₃P₂) is a novel photovoltaic (PV) material with a direct band gap of 1.50 eV, a long minority-carrier diffusion length, and strong light absorption in the visible region.^{1–3} In addition, the terrestrial abundance of its constituent elements attracts attention because of the recent interest in developing high-efficiency PV devices using earth-abundant materials.⁴ The superior absorption and bulk electronic properties as well as the potential for low-cost, thin-film fabrication make Zn₃P₂ a promising active material for earth-abundant solar applications.

The growth of high-quality, thin-film Zn₃P₂ for PV applications has been attempted using a variety of techniques such as vacuum deposition, ionized-cluster beam deposition, vapor phase deposition, and hot wall deposition.^{5–9} However, these techniques typically produced polycrystalline films without the necessary electronic material quality to observe the full potential of Zn₃P₂ for photovoltaic applications. To enhance the material quality of Zn₃P₂ thin films, other growth techniques have been reported, including metalorganic vapor phase epitaxy (MOCVD)^{10,11} and molecular-beam epitaxy (MBE).¹² Epitaxial Zn₃P₂ films were also grown by a compound-source MBE technique,¹³ which is possible because Zn₃P₂ sublimates congruently as follows,¹⁴



The compound-source MBE technique was not only simple, due to the fewer number of sources required, but produced films with excellent crystalline quality. However, the detailed chemistry, mechanism, and geometric/electronic structures of this growth process have yet to be thoroughly explored. Understanding the surface and interface properties of a Zn₃P₂ epilayer has important implications on device fabrication and performance. Knowledge of the atomic structure of the epitaxial Zn₃P₂ surface plays a significant role in additional processing steps, for example, the growth of additional epilayers, the design of surface passivation/window layers, and the functionalization/modification of the surface with chemical species. Furthermore, understanding the reaction chemistry and electronic properties at the interface between Zn₃P₂ and the GaAs substrate significantly contributes to developing functional heterojunction devices.

We report herein the detailed chemical, structural, and electronic properties of the surface and interface of pseudomorphic Zn₃P₂ epilayers grown on the GaAs(001)

Received: December 30, 2013

Revised: May 6, 2014

Published: May 16, 2014

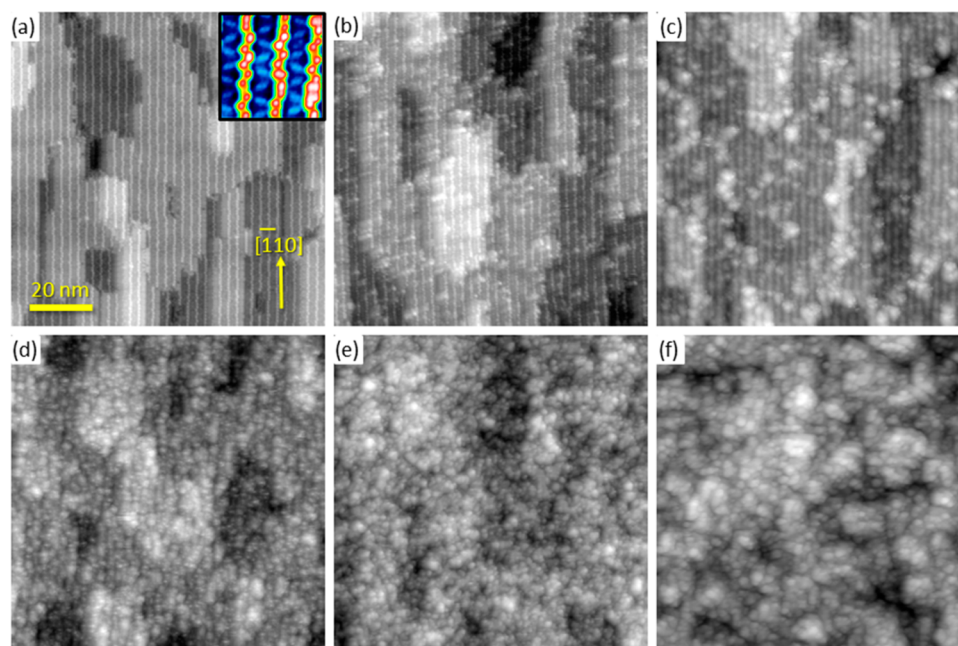


Figure 1. STM topography images of (a) the clean GaAs(001)-(6 × 6) surface and Zn₃P₂/GaAs(001) surface grown at 180 °C with various amounts of exposure: (b) 0.05 L, (c) 0.2 L, (d) 0.63 L, (e) 0.95 L, and (f) 3.4 L. The image size of the inset of panel a is 7.5 nm².

surface. High-resolution scanning tunneling microscopy (STM) and X-ray photoelectron spectroscopy (XPS) were employed to elucidate the geometric and electronic structure of the Zn₃P₂ films at the initial growth stages under various conditions. Additionally, high-resolution X-ray diffraction (HRXRD) and transmission electron microscopy (TEM) were used to verify the crystallinity and orientation of the as-grown films. The energy-band alignment of the Zn₃P₂ epilayer with respect to the GaAs substrate was determined based on thickness-dependent XPS measurements. Finally, the formation of a thin GaP layer at the interface between Zn₃P₂ and GaAs was corroborated by scanning tunneling spectroscopy (STS), XPS, and TEM data, as well as density functional theory (DFT) calculations. The impact of the observed morphological and electronic properties of the Zn₃P₂/GaAs interface on the construction of Zn₃P₂ solar cells is discussed.

2.0. EXPERIMENTAL AND COMPUTATIONAL DETAILS

2.1. Zn₃P₂ Film Growth. The growth of Zn₃P₂ epilayers on the Ga-rich GaAs(001) substrate was carried out in an ultrahigh vacuum (UHV) molecular-beam epitaxy (MBE) chamber (base pressure of $<1 \times 10^{-10}$ Torr). We used n-type GaAs(001) single-crystal wafers (carrier density $\sim 1 \times 10^{18}$ cm⁻³, AXT Inc.) as epi-ready substrates. The surface of the substrate was cleaned by several cycles of Ne⁺ ion bombardment (500 eV) and annealing (530 °C) in the UHV chamber. In the final cycle, the annealed surface was slowly ramped down with the cooling rate of $-1 \sim -2$ °C s⁻¹. A Ga-rich GaAs(001)-(6 × 6) surface reconstruction was reliably obtained, which was verified by STM. The (6 × 6) surface did *not* contain excess Ga droplets which would have indicated an undesirable increase of the surface Ga/As atomic ratio. Zn₃P₂ epilayers were grown on the clean, well-defined (6 × 6) surface at the normal growth temperature (180 °C) and various high temperatures (≥ 300 °C) using the compound-source MBE technique.¹³ The Zn₃P₂ flux was maintained by applying a constant power to a Zn₃P₂-loaded effusion cell, which gave the effusion cell temperature of

420 °C and the chamber background pressure of $\sim 1 \times 10^{-9}$ Torr. We expect the pressure of the source beam is roughly 2 orders of magnitude higher than the measured background pressure owing to the position of the nude ion gauge. Every Zn₃P₂/GaAs(001) sample was prepared in one continuous deposition in order to prevent intermittence in the growth which could potentially generate chemical inhomogeneities inside the epilayer. The amount of the Zn₃P₂ deposition is expressed in Langmuir (1 Langmuir (L) = 1×10^{-6} Torr·s). On the basis of the TEM images of the Zn₃P₂/GaAs(001) samples grown by the procedure above, the growth rate was estimated to be less than 0.1 nm per minute.

2.2. Scanning Tunneling Microscopy and Spectroscopy (STM and STS). The STM and STS characterizations were carried out in a separate UHV chamber (base pressure of $\sim 2 \times 10^{-11}$ Torr) which was connected directly to the MBE chamber by a UHV sample transfer system. The analysis of the surface topography was carried out using a commercial STM (VT-STM XA, Omicron Nanotechnology). The filled-state STM images were obtained under constant-current mode with the sample bias voltage varied between -2.5 and -3.0 V and a set-point current of 100 pA. The tunneling spectra (tunneling current vs sample bias; I - V curve) were acquired from a given feature on the STM images at a fixed sample-to-tip distance which was defined by fixing the bias voltage to -2.5 V and set-point current to 100 pA. A number of I - V curves from the same feature were averaged, and the dI/dV curves were obtained by differentiation. All STM and STS data were taken at room temperature after cooling down the as-grown Zn₃P₂/GaAs(001) films in the STM chamber.

2.3. X-ray Photoelectron Spectroscopy (XPS). XPS measurements were carried out in a Kratos Ultra DLD spectrometer (base pressure of $<3 \times 10^{-9}$ Torr) with a monochromatic Al $K\alpha$ radiation source ($h\nu = 1486.58$ eV). The Zn₃P₂/GaAs(001) samples were transferred from the MBE chamber to the XPS chamber in a portable, stainless-steel chamber filled with anhydrous nitrogen gas. Thus, the sample

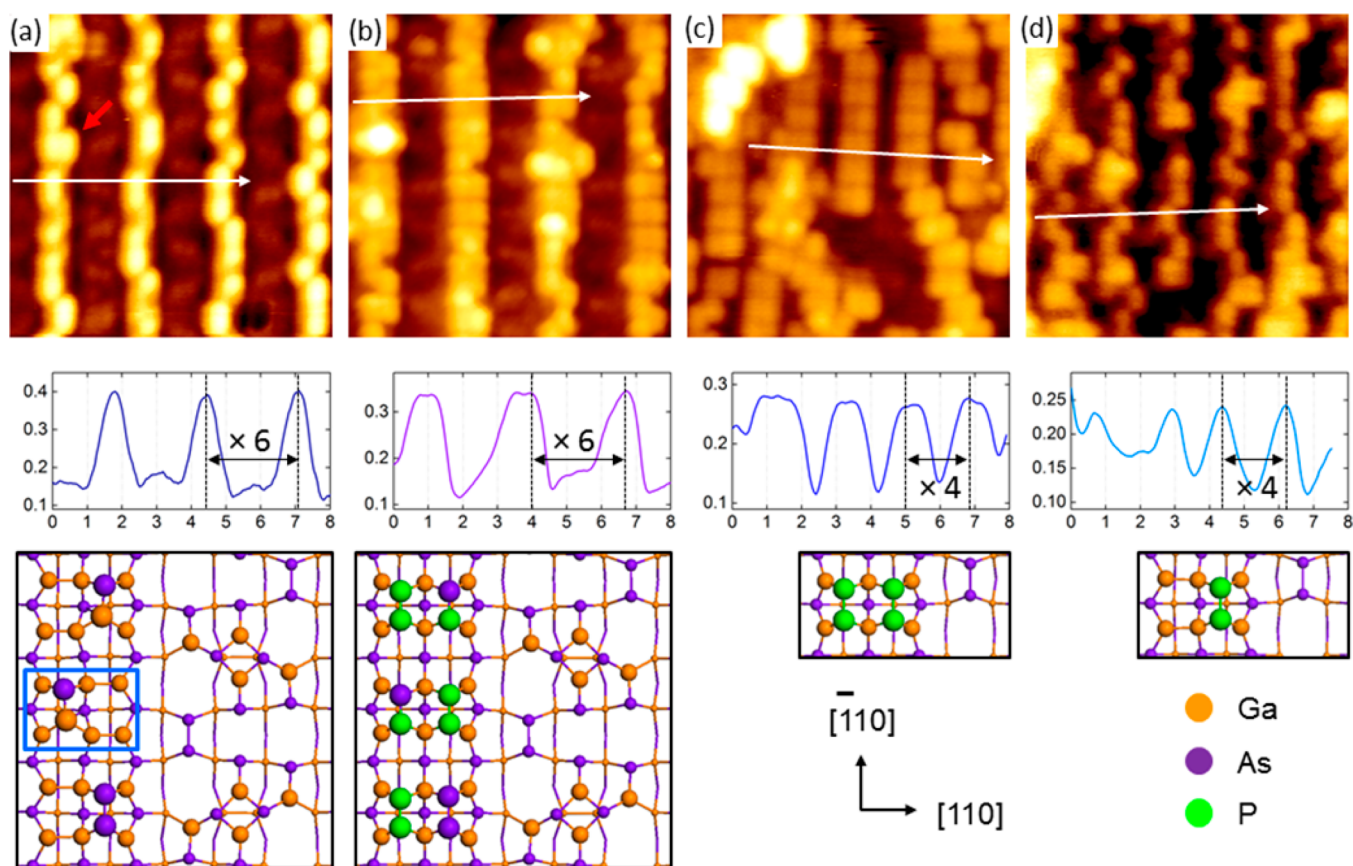


Figure 2. STM topography images (size 10 nm^2), cross section line profiles, and proposed structure models of the $\text{Zn}_3\text{P}_2/\text{GaAs}(001)$ surface grown at different conditions: (a) clean $\text{GaAs}(001)-(6 \times 6)$, (b) 0.14 L at $300 \text{ }^\circ\text{C}$, (c) 3.7 L at $490 \text{ }^\circ\text{C}$, and (d) 3 L at $560 \text{ }^\circ\text{C}$. The red arrow and blue rectangle in column a indicate double As–As dimers in the first layer and (1×2) Ga rectangle in the second layer, respectively.

was not exposed to ambient during transportation. High-resolution spectra were collected at a fixed analyzer pass energy of 20 eV and step size of 25 meV . With this setup, Au $4f$ peaks demonstrated a full width at half maximum (FWHM) value of $0.50\sim 0.51 \text{ eV}$ after fitting to a Gaussian–Lorentzian product function (see Figure S1 of the Supporting Information). The spectra were collected at 0° with respect to the surface-normal direction. The binding energy was referenced to the instrument Fermi level which was calibrated using the Au $4f$ level (84.00 eV) of a clean gold surface. The XPS data were analyzed with the CasaXPS (version 2.3.16) commercial software package. The individual peaks were fit to a Gaussian–Lorentzian product function after a Shirley-type background subtraction. Spin–orbit splittings and branching ratios were held constant at 865 meV and 0.5 for the P $2p$ core level and 701 meV and 0.666 for the As $3d$ core level, respectively.

2.4. Density Functional Theory (DFT). DFT calculations were carried out using the Perdew–Burke–Ernzerhof (PBE) exchange–correlation functional. These calculations replaced the Ar core of Ga, the Ne core of P, and the He core of O with projected augmented-wave (PAW) potentials optimized for the PBE functionals. Thus, Ga was described with three valence electrons, P with five, and O with six. All calculations were performed using the Vienna Ab-initio Simulation Package (VASP). The electronic wave functions were expanded in a plane-wave basis set using a cutoff energy of 380 eV , and the reciprocal space was sampled using k points generated by a $4 \times 2 \times 1$ Monkhorst–Pack scheme. The convergence criteria for electronic and ionic optimization were set to 1×10^{-4} and $1 \times$

10^{-3} eV , respectively. The lattice parameters for the slab calculation were determined from a separate calculation of bulk GaAs for which the cubic lattice constant was optimized as 0.575 nm . The Ga-rich $\text{GaAs}(001)-\beta 2(2 \times 4)$ surface was modeled using a periodic slab geometry composed of four Ga and five As layers with a vacuum region equivalent to eight Ga and As layers, resulting in the composition of the simulation cell as 30 Ga and 36 As atoms. All atomic positions were optimized except for the bottom two Ga and As layers which were fixed. The bottom As layer was passivated with $0.75e^-$ pseudohydrogen atoms to avoid any possible artificial electrostatic force due to spurious charge separation.¹⁵

3.0. RESULT AND DISCUSSIONS

3.1. STM Characterization. Figure 1 shows STM images of Zn_3P_2 epilayers grown on the Ga-rich $\text{GaAs}(001)-(6 \times 6)$ surface at various coverages while maintaining the substrate temperature at $180 \text{ }^\circ\text{C}$. The inset in Figure 1a (also refer to Figure 2a) shows a high-resolution STM image of the $\text{GaAs}(001)-(6 \times 6)$ reconstruction. Each red protrusion at high topographic location along the surface-normal direction was attributed to the As atom of the first atomic layer Ga–As or As–As dimer. The As atom of the Ga–As dimer has one filled dangling bond which protrudes out of the surface, which was seen as a single bright dot in the STM image. The two neighboring As atoms on the As–As dimer were seen as a peanut-shaped feature due to two filled dangling bonds on the dimer. The array of these Ga–As or As–As dimers along the $[-110]$ direction formed a Ga–As or As–As dimer row on the

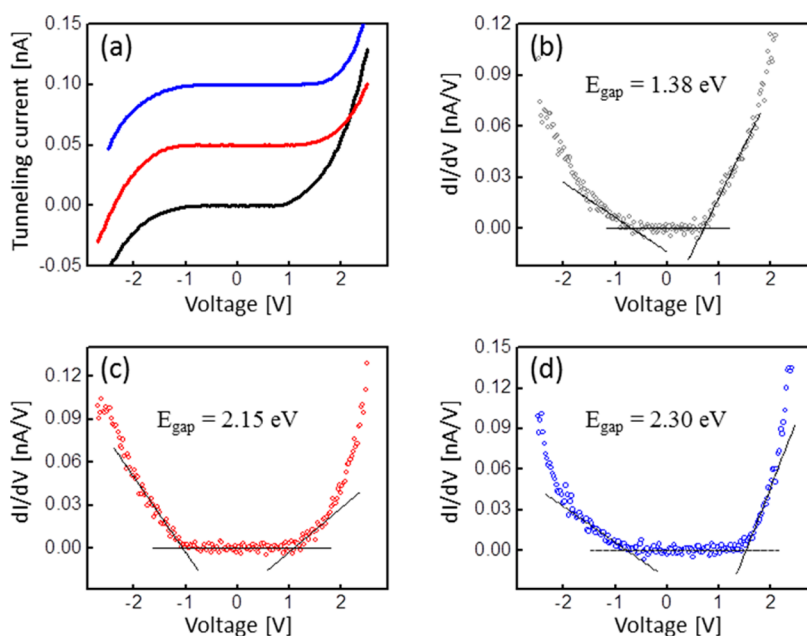


Figure 3. (a) Tunneling current vs sample voltage (I - V) spectra obtained from clean GaAs(001)-(6×6) [black], 3.7 L Zn_3P_2 /GaAs(001) at 490 °C [red], and 13 L Zn_3P_2 /GaAs(001) at 180 °C [blue]. (b-d) The dI/dV vs V curve of each I - V spectrum in panel a. The black lines in panels b-d indicate the linear extrapolation of the leading edges of the dI/dV vs V curves. The displayed number above the dI/dV curve is the apparent band gap which was determined by three linear extrapolation lines.

first atomic layer. The atoms in the blue area between the red dimer rows were located in the second and third atomic layer from the top. The zigzag features in light blue were associated with As atoms of the Ga-As dimers in the blue area. The Ga-As or As-As dimer rows in the first layer and the zigzag features in the second and third layer are signatures of the (6×6) reconstruction in an STM image.^{16,17} The gray STM image in Figure 1a shows not only the large-scale picture of atomic steps and terraces but also the small-scale Ga-As or As-As dimer rows running along $[-110]$ direction. The shape, density, and distribution of the steps and terraces were consistent over different samples after our surface cleaning procedures.

Upon exposure of the clean (6×6) surface to a small overpressure of Zn_3P_2 (≤ 0.2 L), the surface showed bright protrusions at random locations in addition to the clean (6×6) features (Figure 1b and 1c). The size and density of the protrusions increased with increasing deposition amount and were therefore assumed to be Zn_3P_2 nucleation points, or seeds. For epitaxy on the (001) face following the island growth mechanism,¹⁸ the islands are usually seen as square or rectangular shapes at the initial growth stage due to the continuity of bond symmetry between the epilayer and substrate along $[001]$ direction.^{16,19} The shape and size of the islands in the Zn_3P_2 film were irregular and featureless. In addition, STM images collected at higher Zn_3P_2 exposures (Figures 1d and 1e) showed that the islands did not grow to form larger islands or films, but instead the number density increased. The height of the islands had a wide distribution and did not exhibit discrete multiples of an atomic step size of Zn_3P_2 .

To check whether the Zn_3P_2 epilayer was crystalline, HRXRD patterns and TEM images of the Zn_3P_2 /GaAs samples were collected (see Figures S2 and S3 of the Supporting Information). Surprisingly, the data clearly demonstrated that the Zn_3P_2 films were crystalline and pseudomorphic in nature

with growth occurring along the (001) direction of the tetragonal Zn_3P_2 lattice. This indicated that the Zn_3P_2 film must have had a crystalline phase directly beneath the irregularly shaped overlayer observed in the STM images. Figure 1f displays an STM image of a thick (a few nanometers) Zn_3P_2 layer. Again the irregular surface features persisted independent of the film thickness. We note that the irregular-shaped surface features observed in the STM images were not associated with artifacts due to a blunt or molecule-coated tip. Single-atom-sized STM features were clearly observed in high-magnification STM images of the irregular surface but atomic lattice features could not be identified. Such a featureless topography even in high-resolution STM images is very similar to that typically observed for an amorphous phase.²⁰

Figure 2 shows high-resolution STM images (top), cross-sectional line profiles (center), and proposed structure models (bottom) of a clean GaAs(001)-(6×6) surface and submonolayer Zn_3P_2 layers grown on the clean (6×6) surface at high temperatures (300, 490, and 560 °C). Our XPS data showed that the films grown at >400 °C did not contain Zn, which is supported by previous reports of Zn desorption occurring below 323 °C, depending on the coverage and surface properties.^{21,22} Thus, we expect that the films grown at high temperatures are effectively the same as those formed using only an elemental P_4 source. Figure 2a displays the clean GaAs(001)-(6×6) surface reconstruction. The cross-sectional line profile shows the lateral distance along $[110]$ between two neighboring Ga-As or As-As dimer rows was six times larger than the dimension of the surface unit cell. In the structural model, the first-layer Ga-As or As-As dimer sits on top of the six, second-layer Ga atoms shown in the blue rectangle of Figure 2a. Within the rectangle, there exist two locations a Ga-As or As-As dimer can occupy. Sometimes, both of the locations were occupied simultaneously by two Ga-As or As-As dimers—seen as a double peanut-shaped feature (red arrow in Figure 2a). However, the population of the double

peanut-shaped feature was less than $2.62 \pm 1.90\%$ based on five high-resolution STM images that were collected from different samples prepared on different dates. Thus, in most cases only one of the two locations was occupied by a single Ga–As or As–As dimer.

When 0.14 L of Zn_3P_2 was deposited on the clean (6×6) surface at 300°C , the number of double peanut-shaped features increased on the first-layer dimer rows (Figure 2b). Upon exposure of the clean (6×6) surface to a Zn_3P_2 source, any additional feature whose number density increased as the amount of Zn_3P_2 exposure increased was associated with either Zn or P atoms. However, since the peanut-shaped features were also observed on the films grown at temperatures higher than the Zn desorption temperature,^{21,22} Zn was not associated with this surface reconstruction. In addition, since Zn and Ga are cations in II–V and III–V materials, one would expect to observe only the group-V atoms and not the metal atoms in the filled-state STM image under a negative sample voltage. For instance, the Ga atom of the Ga–As dimer on the GaAs(001)- (6×6) reconstruction is not observed at negative voltages (Figure 1a and 2a). Thus, the additional bright protrusions on the first-layer dimer rows post- Zn_3P_2 exposure were associated with As or P atoms. Namely, the double peanut-shaped feature is assigned to As–As, As–P, or P–P dimers.

Figure 2c displays the GaAs surface after 3.7 L of Zn_3P_2 was deposited at 490°C . Interestingly, the interdimer row distance along the $[110]$ direction was decreased from $\times 6$ to $\times 4$ while maintaining the double peanut-shaped features. The growth temperature of 490°C is the temperature at which desorption of As from GaAs(001)- (2×4) ,²³ and formation of the GaP(001)- $\beta 2(2 \times 4)$ surface reconstruction were previously observed.²⁴ Thus, persistence of the double peanut-shaped feature was attributed to replacement of As by P to form P–P dimer rows within the GaP(001)- $\beta 2(2 \times 4)$ reconstruction. Among the stable GaP(001) surface reconstructions, the symmetry and shape of the double peanut-shaped P–P dimer rows with (2×4) symmetry is characteristic of the GaP(001)- $\beta 2(2 \times 4)$ reconstruction.²⁵

Finally, we exposed the GaAs(001) surface to Zn_3P_2 flux at 560°C (Figure 2d). Most of the dimer rows were composed of single peanut-shaped features in a (2×4) unit cell. The line profile showed the interdimer row distance along the $[110]$ direction had $\times 4$ symmetry. Among the GaP(001)- (2×4) reconstructions, which are both theoretically stable and experimentally observable,²⁶ the single peanut-shaped feature with the (2×4) symmetry was associated with GaP(001)- $\delta(2 \times 4)$. The transition from the $\beta 2$ to the δ phase under group-V overpressure at high temperature has been observed previously by STM in a similar system.²⁷

3.2. STS Characterization. The three curves in Figure 3a are tunneling spectra (tunneling current vs sample bias curves; I – V curves) obtained from (i) the first-layer Ga–As or As–As dimer on the clean GaAs(001)- (6×6) surface (black), (ii) the first-layer P–P, P–As, or As–As dimer on the 3.7 L $\text{Zn}_3\text{P}_2/\text{GaAs}(001)$ epilayer grown at 490°C (red), and (iii) an arbitrary feature on the 13 L $\text{Zn}_3\text{P}_2/\text{GaAs}(001)$ epilayer grown at 180°C (blue), respectively. For the last sample, there was no periodic STM feature on the surface as shown in Figure 1f. Therefore, the tunneling spectra were collected from arbitrary locations on the surface. A substantial number of I – V curves were collected from each surface, averaged, and then differentiated to produce dI/dV curves. The dI/dV from tunneling spectroscopy is proportional to the local density of states at the

surface.²⁸ The positions of the valence-band maximum and conduction-band minimum for each surface were determined by linear extrapolation of the leading edges of the dI/dV curve. The apparent band gaps, which were calculated as the difference between the valence-band and conduction-band edges, are also displayed in Figure 3b–d.

The apparent band gap of 1.38 eV collected for the clean GaAs(001)- (6×6) surface was in excellent agreement with the known GaAs bulk band gap of 1.42 eV (Figure 3b). In addition, since the Fermi level ($V_{\text{sample}} = 0$) was located in the middle of the band gap in spite of the substrate's high n-doping level ($N_d \approx 1 \times 10^{18} \text{ cm}^{-3}$), the (6×6) surface prepared by the inert-gas ion bombardment and annealing method in this study demonstrated Fermi-level pinning. On the basis of the literature, Fermi-level pinning is strongly dependent on the surface structure and defects which are influenced by the surface preparation method, the type of reconstruction, and the type and density of defects, etc. Therefore, contradictory results are common among different studies in which the Fermi level is observed to be pinned and unpinned for a given surface reconstruction.^{29,30}

Exposure of the clean surface to Zn_3P_2 flux caused substantial changes in the observed tunneling spectra. The dI/dV obtained from $\text{Zn}_3\text{P}_2/\text{GaAs}(001)$ grown at 490°C displayed an apparent band gap of 2.15 eV and evidence of Fermi-level pinning at the mid gap (Figure 3c). The band gap was significantly different from the known crystalline Zn_3P_2 band gap of 1.50 eV.^{1,13} Instead, the large band gap on this surface was close to the known band gap of GaP of 2.26 eV. Therefore, the scanning tunneling spectra supported the formation of a GaP layer on the GaAs(001) surface when exposed to Zn_3P_2 at high temperatures.

Finally, the tunneling spectra obtained from $\text{Zn}_3\text{P}_2/\text{GaAs}(001)$ grown at 180°C (Figure 3d) demonstrated an apparent band gap of 2.30 eV which was again significantly larger than the established Zn_3P_2 band gap. The larger apparent band gap was attributed to the surface overlayer phase composed of amorphous zinc phosphide (a-ZnP_x ; $x > 1$) and elemental P. The band gap of ZnP_2 of 1.44–2.60 eV³¹ indicates that an increased P/Zn atomic ratio is likely one source of the band gap increase in the amorphous layer. Thus, our STS data supports a model suggesting that the overlayer was composed of P-rich amorphous ZnP_x and/or elemental P and that epitaxial Zn_3P_2 growth occurred beneath this layer. However, the position of the Fermi level close to the valence-band edge indicates p-type doping, which was consistent with previous reports.¹³

3.3. XPS Characterization. Figure 4 shows the fitted X-ray photoelectron spectra of the P $2p$ core level collected on Zn_3P_2 epilayers grown at various surface coverages and temperatures. The Zn_3P_2 epilayers in Figure 4a,b were grown at 180°C (normal growth temperature). The P $2p$ region was fitted with three discrete bonding states: (1) a crystalline Zn_3P_2 state ($c\text{-Zn}_3\text{P}_2$), (2) a P-rich a-ZnP_x state, ($x > 1$; +0.55 eV vs $c\text{-Zn}_3\text{P}_2$), and (3) an elemental P state (+1.4 eV vs $c\text{-Zn}_3\text{P}_2$). The a-ZnP_x state existed throughout all Zn_3P_2 coverages as shown in the thickness-dependent XPS data in Figure 5a. We note that the FWHM of the a-ZnP_x peak at ≤ 1.1 L was 30% larger than coverages of ≥ 2.1 L. We propose that this was due to the existence of a GaP state (+0.7 eV vs $c\text{-Zn}_3\text{P}_2$) at ≤ 1.1 L with slightly higher binding energy shift than the a-ZnP_x phase. We will discuss the details of the GaP state later. The core-level binding energy shift of +0.55 eV in the a-ZnP_x phase was likely due to disordered bonding which includes P–P and Zn–Zn

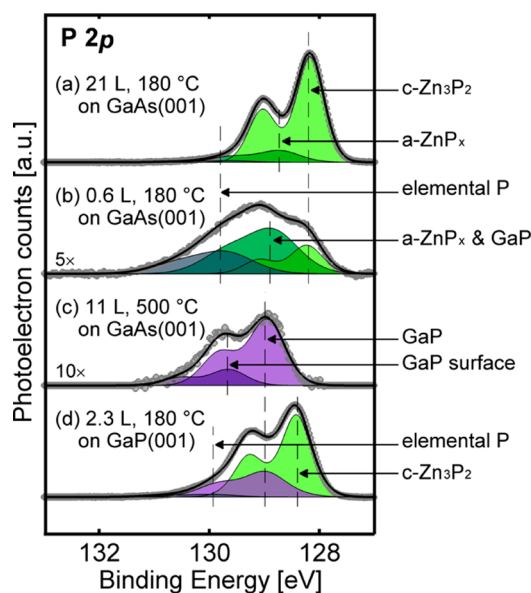


Figure 4. P 2*p* core-level X-ray photoelectron spectra of the Zn₃P₂ film grown at various depositions and substrate temperatures: (a) 21 L and (b) 0.6 L Zn₃P₂ grown on the Ga-rich GaAs(001)-(6 × 6) at 180 °C; (c) 11 L Zn₃P₂ grown on the Ga-rich GaAs(001)-(6 × 6) at 500 °C; (d) 2.3 L Zn₃P₂ grown on the Ga-rich GaP(001)(2 × 4) at 180 °C. Gray circles, black curves, and colorful curves represent raw data, sum of the fitted components, and each displayed components, respectively.

bonds. It has been proposed that ~25% of atoms in an amorphous III–V system exhibit disordered bonding.³² The P atom in the crystalline Zn₃P₂ has four or six bonds with the neighboring Zn atoms. Since Zn has a lower electronegativity than P, the formation of P–P bonds rather than P–Zn bonds in the a-ZnP_x overlayer shifts the P 2*p* core-level binding energy to a higher value. The STM and tunneling spectroscopy data also supported the existence of the P-rich a-ZnP_x overlayer which has a featureless surface morphology and a larger apparent band gap than c-Zn₃P₂.

The third component with the highest binding energy shift of +1.4 eV was attributed to an elemental P layer. The existence of

the phase and the binding energy shift of the elemental P are evident from previous reports.^{33,34} Figure 4c shows the fitted P 2*p* region of the 11 L Zn₃P₂/GaAs(001) sample grown at 500 °C. The P 2*p* region was fitted with two discrete components; a GaP state (+0.7 eV vs c-Zn₃P₂) and a GaP surface state (+1.3 eV vs c-Zn₃P₂). The assignment of the GaP state is based on the P 2*p* core-level binding energy of bulk GaP in the literature.³⁵ The GaP surface state was associated with the P–P and As–P dimers on the surface. The GaAs substrate in this experiment began with well-defined GaAs(001)-(6 × 6) surface structure. The formation of a GaP interfacial layer was likely due to either the reaction of P with the Ga adatoms on the Ga-rich surface or anion replacement of subsurface As with P atoms prior to or during epilayer growth. The coverage of the GaP layer in the Zn₃P₂ grown on GaAs(001) over 300 °C did not exceed 1 ML (monolayer) based on our quantitative analysis of the XPS data, despite Zn₃P₂ exposures as high as 18 L, which agreed with previous results.³⁶

To verify the binding energy shift of the GaP state with respect to the c-Zn₃P₂ state, photoelectron spectra were collected on Zn₃P₂ films grown directly on a single crystal GaP(001) substrate. The Ga-rich GaP(001)-(2 × 4) surface was prepared by the inert-gas ion bombardment and annealing method, which was confirmed by STM image analysis.³⁷ Figure 4d shows fitted photoelectron spectra of the P 2*p* region from a Zn₃P₂ film grown on the Ga-rich GaP(001) surface at 180 °C. There were three components in this region: a c-Zn₃P₂ state, a GaP state (+0.5 eV vs c-Zn₃P₂), and an elemental P state (+1.3 eV vs c-Zn₃P₂). The binding energy of the GaP state in the Zn₃P₂/GaP(001) system was consistent with that of the GaP layer present in the Zn₃P₂/GaAs(001) grown at 500 °C in Figure 4c. Thus, the existence of a GaP state for interfaces grown at high temperatures was supported by several independent observations. On the other hand, existence of the GaP interface at the normal growth temperature (180 °C) was difficult to substantiate with the XPS data alone. This was because (1) the amount of P in the GaP layer was very small (≤1 ML) and therefore difficult to observe and (2) the GaP binding energy shift of +0.7 eV was too close to separate from the B.E. shift of +0.55 eV of the a-ZnP_x state. However, in the STM experiment, we observed P atoms adsorbed on top of the

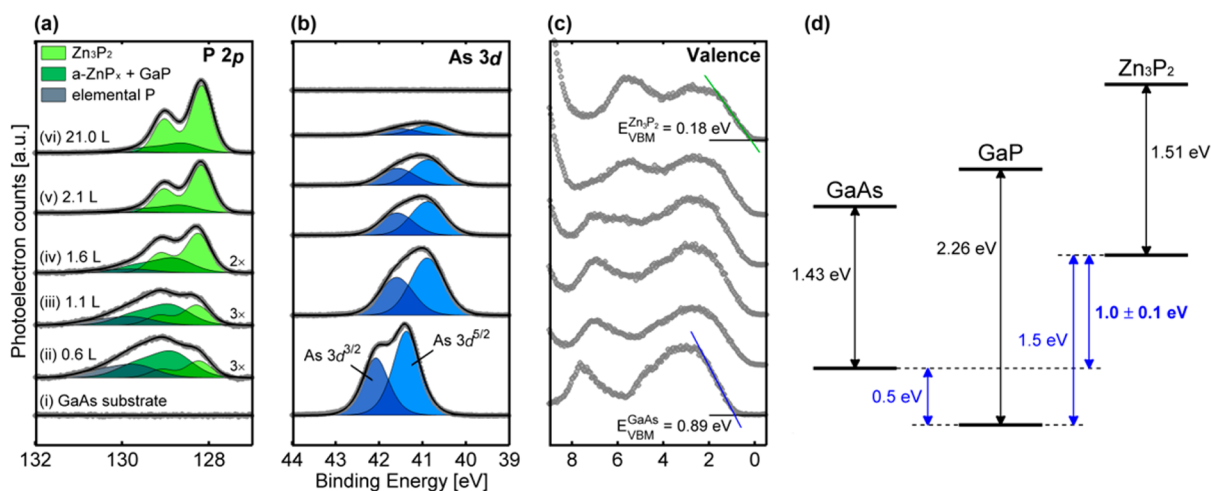


Figure 5. Fitted X-ray photoelectron spectra of the (a) P 2*p* core level, (b) As 3*d* core level, and (c) valence-band region measured on Zn₃P₂/GaAs(001) heterojunction interfaces with increasing overlayer thickness. (d) The energy-band alignment for a Zn₃P₂/GaP/GaAs(001) heterostructure.

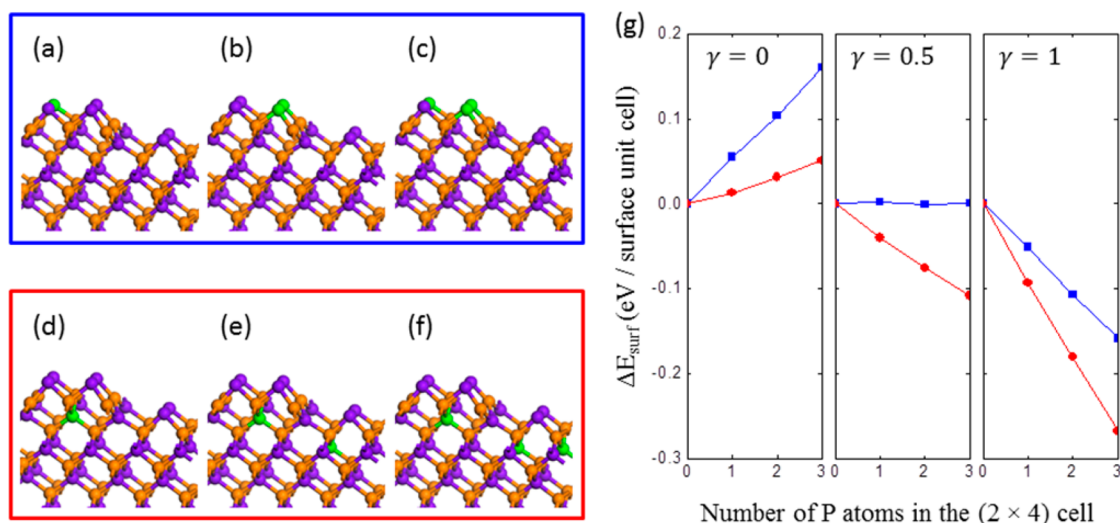


Figure 6. DFT optimized geometries for (a,d) one, (b,e) two, and (c,f) three As replacements by P in the GaAs(001)- $\beta 2(2 \times 4)$ model. The most stable geometries are shown among (a–c) surface and (d–f) subsurface P-replacements at given numbers of P and As atoms in the (2×4) cell. Purple, orange, and green spheres represent As, Ga, and P atoms, respectively. (g) Relative surface formation energy for surface (blue) and subsurface configurations (red) vs the number of P atoms in the GaAs(001)- $\beta 2(2 \times 4)$ cell at three As chemical potentials ($\Delta\mu(\text{As}) = \gamma \cdot \Delta H_f(\text{GaAs})$; $\gamma = 0, 0.5, \text{ and } 1$). The chemical potential of P is fixed ($\Delta\mu(\text{P}) = 0$) (where $\Delta\mu(\text{As}) = \mu(\text{As}) - \mu(\text{As}^{\text{bulk}})$ and $\Delta\mu(\text{P}) = \mu(\text{P}) - \mu(\text{P}^{\text{bulk}})$).

second-layer Ga atoms to form P–P or P–As dimers at initial coverages for both normal growth and high temperatures. In addition, the binding energy shift of the GaP layer in the $\text{Zn}_3\text{P}_2/\text{GaAs}$ grown at high temperature was exactly matched with the known GaP binding energy. Thus, a thin GaP layer existed at the interfacial region between the Zn_3P_2 epilayer and the GaAs(001) substrate. It is surprising that the GaP layer permitted the growth of Zn_3P_2 films that are pseudomorphic, indicating the GaP was itself strained to the in-plane GaAs native lattice constant.

XPS data of the P $2p$ core level, As $3d$ core level, and valence-band region of $\text{Zn}_3\text{P}_2(001)/\text{GaAs}(001)$ interfaces of increasing epilayer thickness are presented in Figure 5a–c. From the XPS data, the $\text{Zn}_3\text{P}_2/\text{GaAs}$ valence-band discontinuity (ΔE_V) for the $\text{Zn}_3\text{P}_2/\text{GaP}/\text{GaAs}(001)$ heterostructure was estimated using the method proposed by Kraut et al.³⁸ This procedure was previously used to determine the valence-band offsets for a series of epitaxial II–VI/ Zn_3P_2 heterojunctions.^{39,40} The offset calculation was supplemented by XPS measurements of Zn_3P_2 epilayers grown directly on the GaP(001) surface under identical conditions. The measured band offsets for the system are displayed in Figure 5d. A value of $\Delta E_V = 1.0 \pm 0.1$ eV was found for the $\text{Zn}_3\text{P}_2/\text{GaAs}$ system. The GaP/GaAs ΔE_V of ~ 0.5 eV was previously obtained from optical measurements on GaP–GaAs quantum well structures.⁴¹ Therefore, assuming the transitivity of band discontinuities is valid for this material system results in a $\text{Zn}_3\text{P}_2/\text{GaP}$ ΔE_V of ~ 1.5 eV.

Equilibrium calculations of the band bending for a $\text{Zn}_3\text{P}_2/\text{GaAs}(001)$ heterostructure with a 1.0 nm thick GaP interfacial layer were performed using the AFORS-HET simulation package.⁴² The calculations showed that the band offset between the Zn_3P_2 and GaAs caused the formation of a hole-blocking layer at the GaAs surface and a hole-accumulation layer at the Zn_3P_2 surface (see Figure S4 of the Supporting Information). It was also found that the GaAs dopant density had a large impact on the width of the hole-blocking layer. A GaAs acceptor concentration of $1 \times 10^{19} \text{ cm}^{-3}$ or greater is likely required before tunneling can occur and suitable ohmic contact between the substrate and Zn_3P_2 epilayer can be made.

Neither the doping concentration of the Zn_3P_2 epilayer nor the GaP interfacial layer had a significant impact on the formation of the hole-blocking layer in the GaAs.

3.4. DFT Calculations. Our STM measurements indicated that exposure of the GaAs(001)- (6×6) surface to a Zn_3P_2 overpressure caused the formation of a GaP(001)- $\beta 2(2 \times 4)$ surface reconstruction at 490 °C. Tunneling spectroscopy and XPS of the P $2p$ and Zn $2p$ regions on the (2×4) surface showed the formation of a GaP layer with the P surface coverage limited to <1 ML and with no Zn adsorption. Since there was no Zn present, the transition from a (6×6) to a (2×4) symmetry was attributed to P adsorption which lead to the formation of one additional P–P or P–As dimer row per (6×6) surface unit cell. However, the additional P atoms could have also incorporated into the subsurface layers of the GaAs in addition to surface adsorption. High growth temperatures of >490 °C likely created favorable conditions to overcome the energy barrier of the subsurface anion replacement reaction.

To understand the energetics for the anion replacement of As by P on the surface and within the subsurface of the (2×4) reconstruction, we employed density functional theory (DFT) calculations. A periodic supercell model was built and optimized to describe the GaAs(001)- $\beta 2(2 \times 4)$ reconstruction whose energy was set as the reference. We then studied the thermodynamics of the anion replacement reaction. Although it would be useful to simulate P adsorption and replacement reactions on all observed surface reconstructions, such as the (6×6) , $\beta 2(2 \times 4)$, and $\delta(2 \times 4)$, we chose to limit our study to the $\beta 2(2 \times 4)$ surface reconstruction.

To compare the energetics between the clean GaAs(001)- $\beta 2(2 \times 4)$ and the P-replaced $\beta 2(2 \times 4)$ structures and their dependence on the number of substitutions, the surface formation energy was calculated as a function of the P and As chemical potentials (see Supporting Information for calculation details).⁴³ Up to three As atoms were replaced by P atoms according to the following procedure. First, each As atom on the surface or in the subsurface (up to the seventh layer from the top) was replaced by a P atom followed by geometry optimization. After fixing the first P-replacement

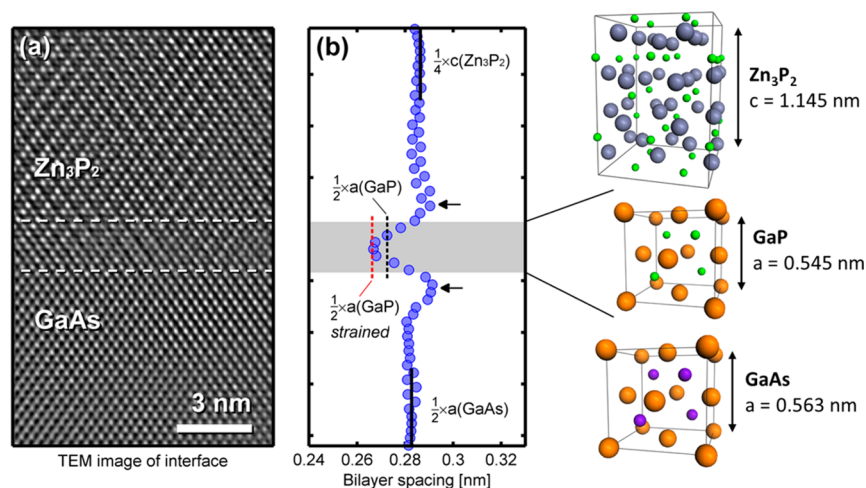


Figure 7. (a) High-resolution TEM image of the Zn₃P₂(001)/GaAs(001) interface showing the presence of a GaP interfacial layer. (b) The calculated bilayer spacing across the interface. The black lines represent the bilayer spacing for the Zn₃P₂ and GaAs lattices. The black and red dotted lines represent the bilayer spacing for unstrained and strained GaP, respectively. Gray, orange, green, and purple spheres in the structure model represent Zn, Ga, P, and As atoms, respectively.

location, we searched for the second P-replacement position. Finally, after fixing the two P-replacement locations which had been selected in the previous step, we searched for the third P-replacement position.

Among the 28 possible cases for the first P-replaced structures, P replacement of the third-layer As atom beneath the center of the surface As dimer block in the first layer (Figure 6d) had the lowest energy. Substitution of the first- or third-layer As atoms which were exposed to vacuum gave less favorable structures whose energies were 331–341 meV higher than the most stable subsurface replacement configuration (compare Figure 6 panel a with panel d). On the other hand, replacement of the third-layer As atom below the first-layer As dimer block was preferred over that of the fifth-layer As atom by 95–153 meV. Thus, replacement of the third-layer As atom under the As dimer block was favored over that of either the surface or deep (below third layer) As atoms.

The most stable structure including two P replacements is shown in Figure 6e. For the surface replacement, formation of a P–P dimer (Figure 6b) was energetically more favorable than two As–P dimers on the first layer by 37–45 meV. Finally, after fixing the locations of the two P atoms, we replaced every As atom located up to the fifth layer by P followed by geometry optimization. The results showed that formation of a Ga–P–Ga–P chain in the third layer on the plane which bisects the surface As dimer block was most energetically favorable (Figure 6f).

A relative surface formation energy diagram, demonstrating the dependence on the number and locations of P replacements, is displayed in Figure 6g. In our experiments, we exposed the GaAs surface to a P₄ flux, which was assumed to be an extremely P-rich condition, $\Delta\mu(\text{P}) = 0$ (where $\Delta\mu(\text{P}) = \mu(\text{P}) - \mu(\text{P}^{\text{bulk}})$). On the other hand, the lack of As supply in our experimental condition yields $\Delta\mu(\text{As}) < 0$ (where $\Delta\mu(\text{As}) = \mu(\text{As}) - \mu(\text{As}^{\text{bulk}})$). Figure 6g shows three conditions: extremely As-rich ($\gamma = 0$), intermediate ($\gamma = 0.5$), and As-poor ($\gamma = 1.0$).

The following results are motivated from our DFT simulations. First, at any given As chemical potential, the replacement of As for P in the subsurface region was energetically more favorable than replacement on the surface.

Second, at the experimental conditions reported herein, for example at a low As chemical potential ($\gamma = 0.5$ and 1), replacement of subsurface As by P was exothermic. On the other hand, replacement of surface As for P was exothermic when the As chemical potential was sufficiently low (e.g., $\gamma < 0.5$). Third, the anion replacement was initiated from the third layer that is under the first-layer As dimer block, followed by a second replacement in the fifth layer under the third-layer As–As dimer. Further anion replacement forms a (Ga–P)_n chain structure at the subsurface. Finally, anion replacement occurring at a location deeper than the third layer was energetically less favorable than that on the third layer.

3.5. TEM Characterization. To confirm the existence of the GaP interfacial layer and to estimate its thickness, transmission electron microscopy (TEM) images of the Zn₃P₂/GaAs(001) interface were collected. We note that the GaAs substrate in this TEM analysis was cleaned using an atomic hydrogen source,¹³ which created a rougher and more Ga-rich surface than the GaAs(001)-(6 × 6) prepared by the inert-gas ion bombardment and annealing procedure. Except for the substrate cleaning method, all other growth methods and conditions were identical.

Figure 7a shows a high-resolution TEM image of the Zn₃P₂/GaAs(001) interface revealing crystalline, atomic order with (001) out-of-plane orientation for both the substrate and the epilayer. The out-of-plane bilayer spacing across the interface (Figure 7b) was calculated by averaging the image contrast across the atomic layers and determining the distance. Both the GaAs and Zn₃P₂ bilayer spacings were in excellent agreement with the values calculated from the known lattice constants of each crystal structure (black lines). However, near the interface the bilayer spacing dramatically decreased. The smallest bilayer spacing observed matched the expected spacing of a GaP lattice which was under tensile strain due to the GaAs in-plane lattice constant (red dotted line). We believe this to be evidence of a tetragonally strained GaP interfacial layer between the GaAs substrate and the Zn₃P₂ epilayer. The thickness of the interfacial layer was difficult to accurately determine since changes in the bilayer spacing did not occur in discrete steps. However, the thickness appears to be on the order of 1–2 nm. The thickness of the GaP interface from the TEM analysis was

slightly larger than the thickness estimated by the DFT simulations (up to 3 Ga–P bilayers). This was likely due to deviations in morphology and stoichiometry of the substrate surfaces cleaned by the atomic hydrogen source from the ideal reconstructed surface. Finally, slight increases in the Zn_3P_2 and GaAs bilayer spacings directly adjacent to the interface were also observed (black arrows), indicating that the strained GaP layer caused some tetragonal compressive strain to occur in the adjacent epilayer and substrate.

4.0. CONCLUSIONS

The schematic diagram in Figure 8 displays the proposed film growth mechanism of Zn_3P_2 on the Ga-rich GaAs(001) surface

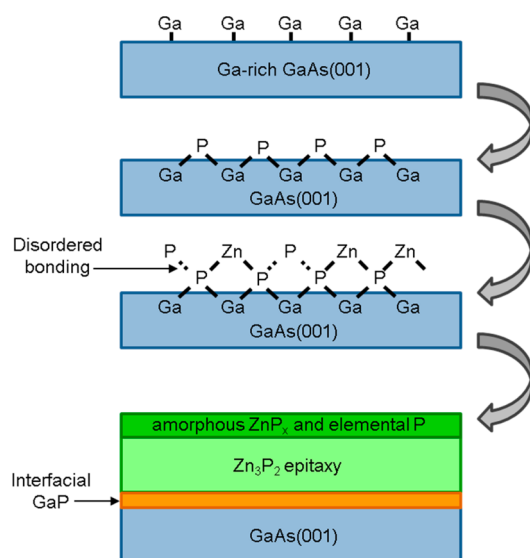


Figure 8. A schematic of the proposed mechanism for Zn_3P_2 epilayer growth on the GaAs(001) surface.

using compound-source MBE. First, P_4 vapor decomposes and bonds to the surface Ga atoms changing the surface to P-abundant GaAs(001). When the growth was carried out at high substrate temperature (≥ 490 °C), the $\beta 2(2 \times 4)$ and $\delta(2 \times 4)$ reconstructions were observed by STM. STS and XPS demonstrated that these surface reconstructions are those of the GaP(001) surface based on the apparent band gap and P $2p$ core-level shift. DFT simulations predicted that the replacement of subsurface As atoms by P atoms is an exothermic process, causing the formation of a GaP interfacial layer up to several monolayers thick. This process was followed by the formation of featureless islands with random location on the surface, indicating the growth of a P-rich ZnP_x ($x > 1$) amorphous overlayer. Under further Zn and P flux, an epitaxial Zn_3P_2 film grows below the amorphous overlayer, which was confirmed by XPS, XRD, and TEM studies. However, the surface of the Zn_3P_2 epilayer remains covered by the amorphous overlayer with a total thickness of ~ 1 nm. Formation of the P-rich overlayer is likely due to the low sticking coefficient of Zn as compared to P on the Ga-rich GaAs(001)- (6×6) surface, especially at low Zn_3P_2 coverage. Thus, the film growth is expected to be limited by Zn adsorption.

It is interesting to note that surface morphology during Zn_3P_2 epilayer growth is drastically different from that typically observed during the growth of III–V and II–VI epitaxial films.

In III–V growth, the epilayer surface is usually characterized by an ordered surface reconstruction.¹⁹ However, in the case of Zn_3P_2 grown by the compound-source MBE technique, even at very initial coverages with low source flux, the formation of ordered epitaxial layers was not observed by STM. At higher adlayer coverages, the surface of the epilayer remains covered by a featureless amorphous layer beneath which a pseudomorphic crystalline film is precipitated. This indicates a rather unusual vapor–solid–solid epitaxial growth mechanism. The persistence of the amorphous overlayer adds some complexity to further processing of the Zn_3P_2 epilayer for device fabrication. The overlayer may be used as a protective cap during post processing, similar to the use of As capping layers. Otherwise, it may require appropriate procedures for its removal prior to chemical functionalization or additional film growth. Future studies will focus on the impact of the amorphous overlayer on the electronic properties of the Zn_3P_2 surface as well as its modification and removal.

■ ASSOCIATED CONTENT

Supporting Information

Au $4f$ core-level spectrum, HRXRD scans, TEM images, and calculated energy band diagrams of interfaces between Zn_3P_2 and GaAs(001). Calculation details of surface formation energies of P-replaced GaAs(001)- $\beta 2(2 \times 4)$ structures. This material is available free of charge via the Internet at <http://pubs.acs.org>.

■ AUTHOR INFORMATION

Corresponding Author

*E-mail: haa@caltech.edu. Tel.: +1-626-395-2197.

Notes

The authors declare no competing financial interest.

■ ACKNOWLEDGMENTS

This work was supported by Dow Chemical Company and by the Department of Energy. S.J. thanks to Kwanjeong Educational Foundation for support. H.K. acknowledges the support by the Global Frontier R&D Program (2013-073298) on Center for Hybrid Interface Materials (HIM) funded by the Ministry of Science, ICT & Future Planning. XPS measurement was carried out in the Molecular Materials Research Center of the Beckman Institute of Caltech.

■ REFERENCES

- (1) Kimball, G. M.; Müller, A. M.; Lewis, N. S.; Atwater, H. A. Photoluminescence-Based Measurements of the Energy Gap and Diffusion Length of Zn_3P_2 . *Appl. Phys. Lett.* **2009**, *95*, 112103–1–3.
- (2) Pawlikowski, J. M. Absorption Edge of Zn_3P_2 . *Phys. Rev. B* **1982**, *26*, 4711–4713.
- (3) Bhushan, M.; Catalano, A. Polycrystalline Zn_3P_2 Schottky Barrier Solar Cells. *Appl. Phys. Lett.* **1981**, *38*, 39–41.
- (4) Wadia, C.; Alivisatos, A. P.; Kammen, D. M. Materials Availability Expands the Opportunity for Large-Scale Photovoltaics Deployment. *Environ. Sci. Technol.* **2009**, *43*, 2072–2077.
- (5) Arsenault, C. J.; Brodie, D. E. Electrical and Optical-Properties of Vacuum-Deposited Amorphous Zn_3P_2 Thin-Films. *Can. J. Phys.* **1987**, *65*, 756–759.
- (6) Babu, V. S.; Vaya, P. R. Studies on Hot Wall Deposited Zn_3P_2 Thin-Film Surfaces and Interfaces. *Appl. Surf. Sci.* **1989**, *37*, 283–290.
- (7) Fuke, S.; Imai, T.; Kawasaki, K.; Kuwahara, K. Substrate Effect on the Deposition of Zn_3P_2 Thin-Films Prepared by a Hot-Wall Method. *J. Appl. Phys.* **1989**, *65*, 564–566.

- (8) Suda, T. Zinc Phosphide Thin-Films Grown by Plasma Assisted Vapor-Phase Deposition. *J. Cryst. Growth* **1990**, *99*, 625–629.
- (9) Suda, T.; Kanno, T.; Kurita, S. Properties of Zn₃P₂ Thin-Films Grown by Ionized-Cluster Beam Deposition. *Jpn. J. Appl. Phys., Part 2* **1983**, *22*, L777–L779.
- (10) Kakishita, K.; Ikeda, S.; Suda, T. Zn₃P₂ Epitaxial-Growth by MOCVD. *J. Cryst. Growth* **1991**, *115*, 793–797.
- (11) Suda, T.; Kakishita, K. Epitaxial-Growth of Zinc Phosphide. *J. Appl. Phys.* **1992**, *71*, 3039–3041.
- (12) Suda, T.; Kakishita, K.; Sato, H.; Sasaki, K. N-type Zinc Phosphide Grown by Molecular Beam Epitaxy. *Appl. Phys. Lett.* **1996**, *69*, 2426–2428.
- (13) Bosco, J. P.; Kimball, G. M.; Lewis, N. S.; Atwater, H. A. Pseudomorphic Growth and Strain Relaxation of α -Zn₃P₂ on GaAs(001) by Molecular Beam Epitaxy. *J. Cryst. Growth* **2013**, *363*, 205–210.
- (14) Schoonmaker, R. C.; Venkiteraman, A. R.; Lee, P. K. The Vaporization of Zinc Phosphide. *J. Phys. Chem.* **1967**, *71*, 2676–2683.
- (15) Shiraishi, K. A New Slab Model Approach for Electronic-Structure Calculation of Polar Semiconductor Surface. *J. Phys. Soc. Jpn.* **1990**, *59*, 3455–3458.
- (16) Kocan, P.; Ohtake, A.; Koguchi, N. Structural Features of Ga-Rich GaAs(001) Surfaces: Scanning Tunneling Microscopy Study. *Phys. Rev. B* **2004**, *70*, 201303–1–4.
- (17) Ohtake, A. Structure and Composition of Ga-Rich (6 × 6) Reconstructions on GaAs(001). *Phys. Rev. B* **2007**, *75*, 153302–1–4.
- (18) Venables, J. A.; Spiller, G. D. T.; Hanbucken, M. Nucleation and Growth of Thin-Films. *Rep. Prog. Phys.* **1984**, *47*, 399–459.
- (19) Xue, Q. K.; Xue, Q. Z.; Hasegawa, Y.; Tsong, I. S. T.; Sakurai, T. Initial Stages of Cubic GaN Growth on the GaAs(001) Surface Studied by Scanning Tunneling Microscopy. *Jpn. J. Appl. Phys., Part 2* **1997**, *36*, L1486–L1489.
- (20) Arima, K.; Kakiuchi, H.; Ikeda, M.; Endo, K.; Morita, M.; Mori, Y. Scanning Tunneling Microscopy/Spectroscopy Observation of Intrinsic Hydrogenated Amorphous Silicon Surface under Light Irradiation. *Surf. Sci.* **2004**, *572*, 449–458.
- (21) Venkateswaran, N.; Roe, C. L.; Lam, H. T.; Vohs, J. M. The Influence of Surface Structure on the Reaction of Dimethylzinc on GaAs(100). *Surf. Sci.* **1996**, *365*, 125–135.
- (22) Laurence, G.; Joyce, B. A.; Foxon, C. T.; Janssen, A. P.; Samuel, G. S.; Venables, J. A. Adsorption-Desorption Studies of Zn on GaAs. *Surf. Sci.* **1977**, *68*, 190–203.
- (23) Yamaguchi, H.; Horikoshi, Y. Surface-Structure Transitions on InAs(001) and GaAs(001) Surfaces. *Phys. Rev. B* **1995**, *51*, 9836–9854.
- (24) Wallart, X. A Combined RHEED and Photoemission Comparison of the GaP and InP(001) (2 × 4) Surface Reconstructions. *Surf. Sci.* **2002**, *506*, 203–212.
- (25) Schmidt, W. G. III-V Compound Semiconductor (001) Surfaces. *Appl. Phys. A: Mater. Sci. Process.* **2002**, *75*, 89–99.
- (26) Frisch, A. M.; Schmidt, W. G.; Bernholc, J.; Pristovsek, M.; Esser, N.; Richter, W. 2 × 4 GaP(001) Surface: Atomic Structure and Optical Anisotropy. *Phys. Rev. B* **1999**, *60*, 2488–2494.
- (27) Li, C. H.; Li, L.; Law, D. C.; Visbeck, S. B.; Hicks, R. F. Arsenic Adsorption and Exchange with Phosphorus on Indium Phosphide (001). *Phys. Rev. B* **2002**, *65*, 205322–1–7.
- (28) Chen, J. C. *Introduction to Scanning Tunneling Microscopy*; Oxford University Press: New York, 2008; p 56.
- (29) Winn, D. L.; Hale, M. J.; Grassman, T. J.; Kummel, A. C.; Droopad, R.; Passlack, M. Direct and Indirect Causes of Fermi Level Pinning at the SiO₂/GaAs Interface. *J. Chem. Phys.* **2007**, *126*, 084703–1–12.
- (30) Gallagher, M. C.; Prince, R. H.; Willis, R. F. On the Atomic-Structure and Electronic-Properties of Decapped GaAs(001)(2 × 4) Surfaces. *Surf. Sci.* **1992**, *275*, 31–40.
- (31) Rud, V. Y.; Rud, Y. V.; Vaipolin, A. A.; Bodnar, I. V.; Osipova, M. A.; Ushakova, T. N. Photosensitive Structures Based on ZnP₂ Single Crystals of Monoclinic and Tetragonal Modifications: Fabrication and Properties. *Semiconductors* **2009**, *43*, 858–864.
- (32) Udron, D.; Flank, A. M.; Gheorghiu, A.; Lagarde, P.; Theye, M. L. Evidence of Chemical Disorder in Amorphous GaP. *Phys. B* **1989**, *158*, 625–626.
- (33) Kadotani, N.; Shimomura, M.; Fukuda, Y. Surface Structure of Phosphorus-Terminated GaP(001)-(2 × 1). *Phys. Rev. B* **2004**, *70*, 165323–1–5.
- (34) Moulder, J. F.; Stickle, W. F.; Sobol, P. E.; Bomben, K. D. *Handbook of X-ray Photoelectron Spectroscopy*; Chastain, J., Ed.; Physical Electronics: MN, 1992.
- (35) Suzuki, Y.; Sanada, N.; Shimomura, A.; Fukuda, Y. High-Resolution XPS Analysis of GaP(001), (111)A, and (111)B Surfaces Passivated by (NH₄)₂S_x Solution. *Appl. Surf. Sci.* **2004**, *235*, 260–266.
- (36) Beaudry, R.; Watkins, S. P.; Xu, X. G.; Yeo, P. Photorefectance Study of Phosphorus Passivation of GaAs (001). *J. Appl. Phys.* **2000**, *87*, 7838–7844.
- (37) Ludge, K.; Vogt, P.; Pulci, O.; Esser, N.; Bechstedt, F.; Richter, W. Clarification of the GaP(001)(2 × 4) Ga-Rich Reconstruction by Scanning Tunneling Microscopy and ab Initio Theory. *Phys. Rev. B* **2000**, *62*, 11046–11049.
- (38) Kraut, E. A.; Grant, R. W.; Waldrop, J. R.; Kowalczyk, S. P. Semiconductor Core-Level to Valence-Band Maximum Binding-Energy Differences: Precise Determination by X-ray Photoelectron Spectroscopy. *Phys. Rev. B* **1983**, *28*, 1965–1977.
- (39) Bosco, J. P.; Demers, S. B.; Kimball, G. M.; Lewis, N. S.; Atwater, H. A. Band Alignment of Epitaxial ZnS/Zn₃P₂ Heterojunctions. *J. Appl. Phys.* **2012**, *112*, 093703–1–6.
- (40) Bosco, J. P.; Scanlon, D. O.; Lewis, N. S.; Atwater, H. A. Energy-Band Alignment of II-VI/Zn₃P₂ Heterojunctions from X-ray Photoemission Spectroscopy. *J. Appl. Phys.* **2013**, *113*, 203705.
- (41) Recio, M.; Armelles, G.; Melendez, J.; Briones, F. Optical-Properties of GaAs/GaP Strained-Layer Superlattices. *J. Appl. Phys.* **1990**, *67*, 2044–2050.
- (42) Stangl, R.; Kriegel, M.; Kirste, S.; Schmidt, M.; Fuhs, W. AFORS-HET, A Numerical PC Program for Simulation of Heterojunction Solar Cells, version 1.2 In *Proc. IEEE Photovolt. Spec. Conf.*, Orlando, FL, USA, Jan 3-7, 2005.
- (43) Jenichen, A.; Engler, C.; Leibiger, G.; Gottschalch, V. Nitrogen Substitutions in GaAs(001) Surfaces: Density-Functional Supercell Calculations of the Surface Stability. *Phys. Status Solidi B* **2005**, *242*, 2820–2832.